Suppression of overcompensation by secondary electrons for negative ion beams in residual gas

Benzheng Chen, Hui Liao, Hui Li, Yongchuan Xiao, Xiuxia Cao, Shengjin Liu, Yanliang Han, and Weidong Chen*

Institute of High Energy Physics, Chinese Academy of Sciences, Beijing 100049, China and Spallation Neutron Source Science Center, Dongguan 523803, China

(Received 12 May 2025; accepted 25 September 2025; published 17 October 2025)

Space charge compensation (SCC) plays a crucial and foundational role in the transport of low-energy ion beams through residual gas, as it effectively mitigates beam divergence caused by space charge forces. At high residual gas pressures, the space charge compensation degree (SCCD) can exceed 100%, a situation referred to as overcompensation. In this study, a model for secondary particle production and tracking has been integrated into a beam optics calculation code to investigate the overcompensation process during the transport of a negative ion beam through residual hydrogen. The impact of secondary electrons, often overlooked, is examined in detail. The findings indicate that electrons predominantly accumulate in the overcompensation region, effectively mitigating overcompensation by leveling the potential and reducing the SCCD. Based on the electron growth rate, the accumulation process is categorized into three stages. Results pertaining to beam parameters reveal that electrons can affect the growth of beam emittance by altering the transverse potential. This research contributes to enhancing our understanding of SCC processes in the low-energy beam transport domain and improving the precision of future beam optics simulations.

DOI: 10.1103/6w2b-hgsm

I. INTRODUCTION

As an important component of the linear accelerator, the low-energy beam transport (LEBT) region [1–3] accelerates ions extracted from the ion source to tens of keV. Relevant beam optics research [3–5] is essential for improving beam quality and designing accelerators in the LEBT. Due to its proximity to the ion source, the LEBT inevitably contains some residual gas. For the acceleration of negative hydrogen ion beams, the accelerated beam particles can ionize the residual gas, leading to the generation of secondary ions, which contribute to space charge compensation (SCC) [6,7]. This process alleviates the space charge effect, reduces beam divergence, and is a key process in the LEBT.

When the residual gas is ionized, both ions and electrons are generated, referred to as secondary ions and electrons in this paper. For a negative hydrogen ion (H^-) beam passing through residual hydrogen (H_2), this gas ionization is described by the reaction

$$H^- + H_2^0 \rightarrow H^- + H_2^+ + e^-. \quad (1)$$

Additionally, electrons can be detached from the beam ion as follows

$$H^- + H_2^0 \rightarrow H^0 + H_2^0 + e^-, \quad (2)$$

$$H^- + H_2^0 \rightarrow H^+ + H_2^0 + 2e^-. \quad (3)$$

The electron detachment produces H^0 (or H^+) and electrons moving with velocities close to that of the beam. If the potential difference between the beam and the boundaries is not high enough to prevent these fast-moving charged particles from escaping, they cannot accumulate in the system and have minimal influence on the compensation process [8,9]. It is the secondary ions (H_2^+) with relatively low energy in reaction (1) that are responsible for the SCC. When the density of H_2^+ is less than that of H^-, the secondary electrons can only stay in the LEBT for only a brief period after generation (< 100 ns for $\Phi = 45$ mm) because they have small mass and will quickly move to the grounded wall driven by the potential field of the H^- beam. In this scenario, secondary electrons are often neglected in beam optics calculations. The compensation time τ, defined as the average time needed for a beam particle with velocity v to interact with the residual gas with density n and generate a secondary ion, is expressed as

*Contact author: chenwd@ihep.ac.cn

Published by the American Physical Society under the terms of the Creative Commons Attribution 4.0 International license. Further distribution of this work must maintain attribution to the author(s) and the published article's title, journal citation, and DOI.

$$\tau = 1/(nv\sigma), \tag{4}$$

where σ is the ionization cross section. The compensation time is also considered the time required for the SCC to build up. Taking the scenario we are discussing as an example, for a negative hydrogen ion beam with energy 50 keV (velocity 3.09×10^6 m/s) in hydrogen with pressure 3.36 mPa (density 8.12×10^{17} m^{-3} at 300 K), the ionization cross section is 3.66×10^{-20} m^2 (see Appendix A), resulting in a compensation time $\tau \sim 11$ μs.

As the space charge compensation degree (SCCD) increases and approaches 100%, the repulsion on the secondary electrons from the electric field weakens. At high residual gas pressures, the density of secondary ions might exceed that of the beam, leading to an SCCD greater than 100% [10,11]. This overcompensation effect is particularly pronounced within a solenoid magnetic field, which impedes the escape of secondary ions in reaction (1). Instead of being attracted by the wall, these secondary electrons are partially confined by the positive potential field, and their influence on the SCC should not be overlooked. Additionally, electrons in reactions (2) and (3) may have enough energy to overcome the positive potential barrier. But if not, their contributions to the SCC should also be considered.

In this paper, the generation and distribution of secondary electrons during the overcompensation process of the negative hydrogen ion beam in high-density residual gas are studied via simulation. A practical beam trajectory calculation code, combined with an additional model for secondary particle generation and tracking, is employed. To determine the effects of secondary electrons on the SCC, we compare the potential field, SCCD, particle distribution and evolution, and beam parameters both with and without electron consideration. The results indicate that the secondary electrons are primarily distributed in the overcompensation region. These electrons can level the potential distribution, bring the SCCD closer to 100%, and effectively reduce the net charge. Consequently, the growth of beam emittance is affected. By incorporating electrons into the simulation, we achieve a more accurate representation of beam optics.

II. SECONDARY PARTICLE TRACKING MODEL

A straightforward method for addressing the SCC is to reduce the charge (or current) of the ion beam by a known or assumed percentage (equal to the SCCD) so that the space charge force on the ions becomes weaker, which is known as the net current model. However, this model relies on an accurate estimation of the SCCD and is not easily applicable to nonuniform pressure. Instead, our simulations involve the actual generation and tracking of secondary particles, which are considered when solving the field using the particle-in-cell method [12–14]. Consequently, the SCCD at varying positions and times can be determined more precisely. This secondary particle tracking model offers a more realistic representation of SCC and is also referred to as the beam plasma model [4,15].

In the simulation, the electric field solving and beam trajectory calculation are accomplished with the IBSimu code [16]. This C++ code is capable of computing potential fields within a specified geometry and tracking particles in electromagnetic fields. To consider the influence of secondary particles, we add a model for secondary particle generation and tracking based on the Monte Carlo method to achieve the SCC. Code benchmarks have been conducted to ensure its correctness (see Appendix B). Additionally, by changing the tracked particle from secondary particles to stripped protons, simulations on the removal of stripped protons produced in LEBT have been successfully conducted [5].

The simulation process is illustrated in Fig. 1.

The blue section on the left involves simulating the beam in a given electromagnetic field using IBSimu, which represents its original and fundamental function. The red section on the right shows how the secondary particles are generated and tracked with this additional model. These two sections operate iteratively to calculate the distribution of all particles, including beam ions and secondary particles, at each time step. The whole simulation advances by Δt in each cycle. The specific steps are as follows: (i) Solve the Laplace equation to determine the initial potential distribution. (ii) Calculate the trajectory and density of the ion beam in the electromagnetic field using the equations of motion. (iii) Solve the Poisson equation to obtain a new potential distribution, where the total charge density is the sum of the charge densities of the ion beam, secondary ions, and secondary electrons, $\rho = \rho_b + \rho_{si} + \rho_{se}$. If the potential converges, proceed to step (4). Otherwise, repeat step (2). (iv) Use the Monte Carlo method to generate new secondary particles on the trajectory of the ion beam based on the ionization cross section (see Appendix A). (v) Calculate the trajectories and densities of all secondary particles in the electromagnetic field within the time step Δt. If the total simulation time exceeds the ion beam pulse width or the distribution of all particles has stabilized, end the simulation. Otherwise, proceed to step (6). (vi) Solve the Poisson equation to determine the potential considering

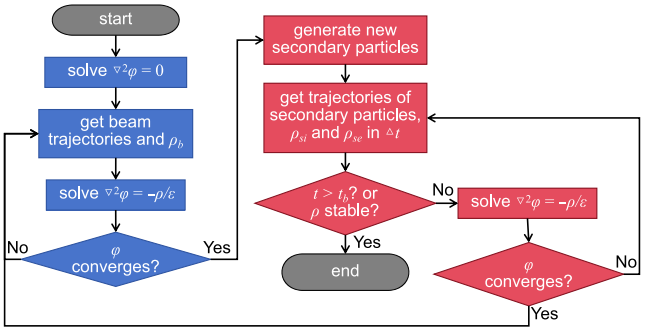


FIG. 1. Flow chart of the beam optics simulation with an additional model for secondary particle generation and tracking.

all charged particles. If the potential converges, proceed to step (2). Otherwise, repeat step (5).

Large time steps ($\Delta t > 5\%\tau$) have been found to potentially lead to numerical instability in simulations. Therefore, a smaller time step of 0.05 μs ($< 0.5\%\tau$) was employed in the following simulations to ensure stability. Secondary particles start with an initial kinetic energy of 0.1 eV. To determine if the simulation reaches an equilibrium state, several quantitative parameters are monitored, including the charge density of particles, SCCD, beam emittance, and particle number.

III. SIMULATION SETTINGS

The simulated region is a 60 mm(x) × 60 mm(y) × 620 mm(z) cuboid filled with uniform hydrogen at 3.36 mPa and 300 K, as shown in Fig. 2(a).

The grid size is 0.5 mm. The boundary conditions in the x and y directions are $\varphi(|x| = 30\ \text{mm}) = 0$ and $\varphi(|y| = 30\ \text{mm}) = 0$. In the z direction, a Neumann boundary condition is applied, implying that the first derivative of the potential with respect to the unit outward normal of the end face remains constant. Particles are removed from the simulation once they reach the boundaries.

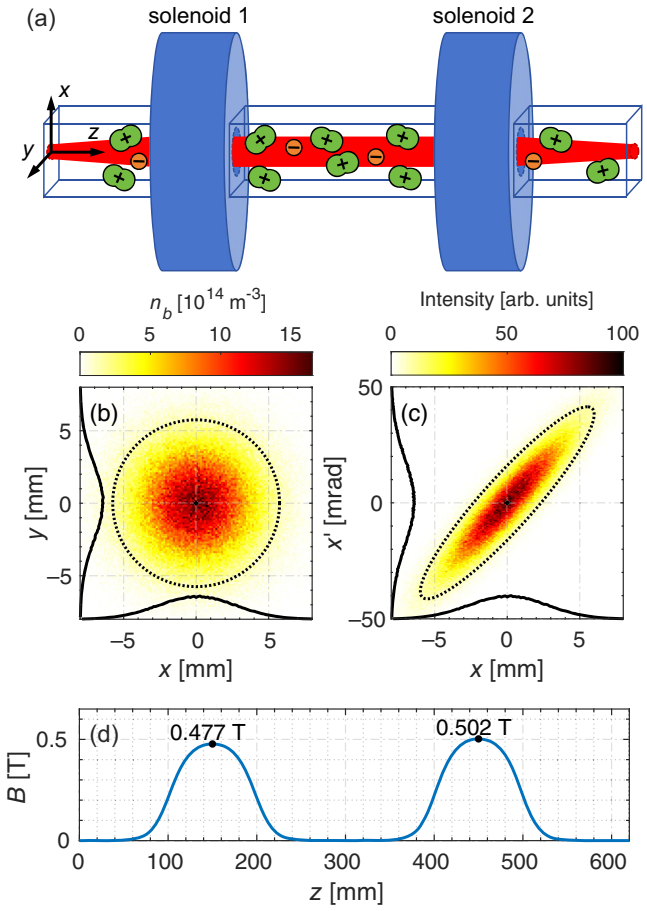


FIG. 2. Several initial settings of the simulation. (a) A schematic diagram of the simulation model. The residual gas is ionized by the beam, generating secondary ions and electrons. (b) Transverse beam density at $z = 0$ with a beam radius of 5.75 mm. (c) The phase space diagram of $x - x'$ at $z = 0$ with rms emittance of 0.199 mm mrad. The dotted curve represents the 5-rms ellipse. (d) The magnetic field along the central axis.

A negative hydrogen ion beam with a current of 40 mA and energy of 50 keV is incident along the z axis. It follows a Gaussian transverse distribution with $\sigma = 3.5$ mm [see Fig. 2(b)]. The beam radius (90% particles included) at the entrance is 5.75 mm, and the central density is 1.65×10^{15} m^{-3}. Figure 2(c) shows the $x - x'$ phase space diagram at $z = 0$, where the transverse normalized root mean square (rms) emittance is $\epsilon_0 = 0.1991$ mm mrad. The Twiss parameters are $\alpha_0 = -2.370$, $\beta_0 = 0.372$ mm/mrad, and $\gamma_0 = 17.768$ mrad/mm.

Two solenoids at $z = 150$ and 450 mm are intended for beam confinement. The corresponding magnetic field along the z axis is depicted in Fig. 2(d), where the peaks are 0.477 and 0.502 T. The divergent beam becomes nearly parallel after the first solenoid and is focused by the second one.

IV. RESULTS AND ANALYSES

A. Potential and SCCD

It is necessary to define the SCCD before discussing its distribution and change. The SCCD can be described in terms of particle charge (or charge density) as

$$\eta = 1 - (N_t e)/(-N_b e) = 1 - \rho/\rho_b, \tag{5}$$

where $N_t e = (N_{si} - N_{se} - N_b)e$ is the total charge, including the charges of secondary ions ($N_{si}e$), electrons ($-N_{se}e$), and beam particles ($-N_b e$). Here, ρ is the total charge density, and ρ_b is the charge density of beam particles. An alternative definition of the SCCD based on potential [17] is

$$\eta = 1 - (\varphi_0 - \varphi)/(\varphi_0 - \varphi_{\text{NC}}), \tag{6}$$

where φ is the observed potential, φ_0 the potential when only electrodes are considered (fully compensated), and φ_{NC} is the potential when electrodes and beam particles are considered (no secondary particles, uncompensated). Notably, overcompensation occurs when $\varphi > \varphi_0$. Equation (6) is applicable throughout space, whereas Eq. (5) is valid only where beam particles are present ($\rho_b \neq 0$). The SCCD discussed in this paper corresponds to the definition provided by Eq. (6).

In our case, the potential at the boundaries in the x and y directions is given as $\varphi_0 = 0$. Consequently, the SCCD can be simplified to

$$\eta = 1 - \varphi/\varphi_{\text{NC}}. \tag{7}$$

In the following discussion, we will compare and discuss two scenarios: one where secondary electrons are not

considered (referred to as case 1) and the other where they are considered (referred to as case 2).

Simulation results indicate that secondary electrons have a negligible impact on the beam envelope. Figures 3(a) and 3(b) are the beam densities and φ_{NC} at the plane $y = 0$ when the steady state is achieved in three different scenarios: (1) without secondary particles (case 0), (2) with secondary ions and without secondary electrons (case 1), and (3) with both secondary ions and electrons (case 2).

The results show obvious beam focusing within the given magnetic fields. In Fig. 3(a1), the transverse size of the beam is larger than the initial beam width due to the strong space charge effect in case 0, even with the magnetic confinement. The focusing becomes much more significant when secondary ions are considered in case 1 [Fig. 3(a2)] and case 2 [Fig. 3(a3)], which exhibit very similar beam density distributions. At $z = 600$ mm, the output beam density is five times greater than at the entrance, with the radius decreasing by approximately 35%. The difference of the radius at $z = 600$ mm in case 1 and case 2 is only 0.07 mm. The low dependence of the beam envelope on electrons can be attributed to the weak space charge effect, resulting from the high degree of charge compensation within the beam.

The distribution of φ_{NC} is determined by the ion beam density, leading to minima of φ_{NC} at different longitudinal positions being on the central axis where the beam density is highest, as shown in Fig. 3(b). On the left boundary, φ_{NC} reaches its lowest value around -530 V at the center ($x = 0$) in all three cases. In Fig. 3(b1), φ_{NC0} rises as

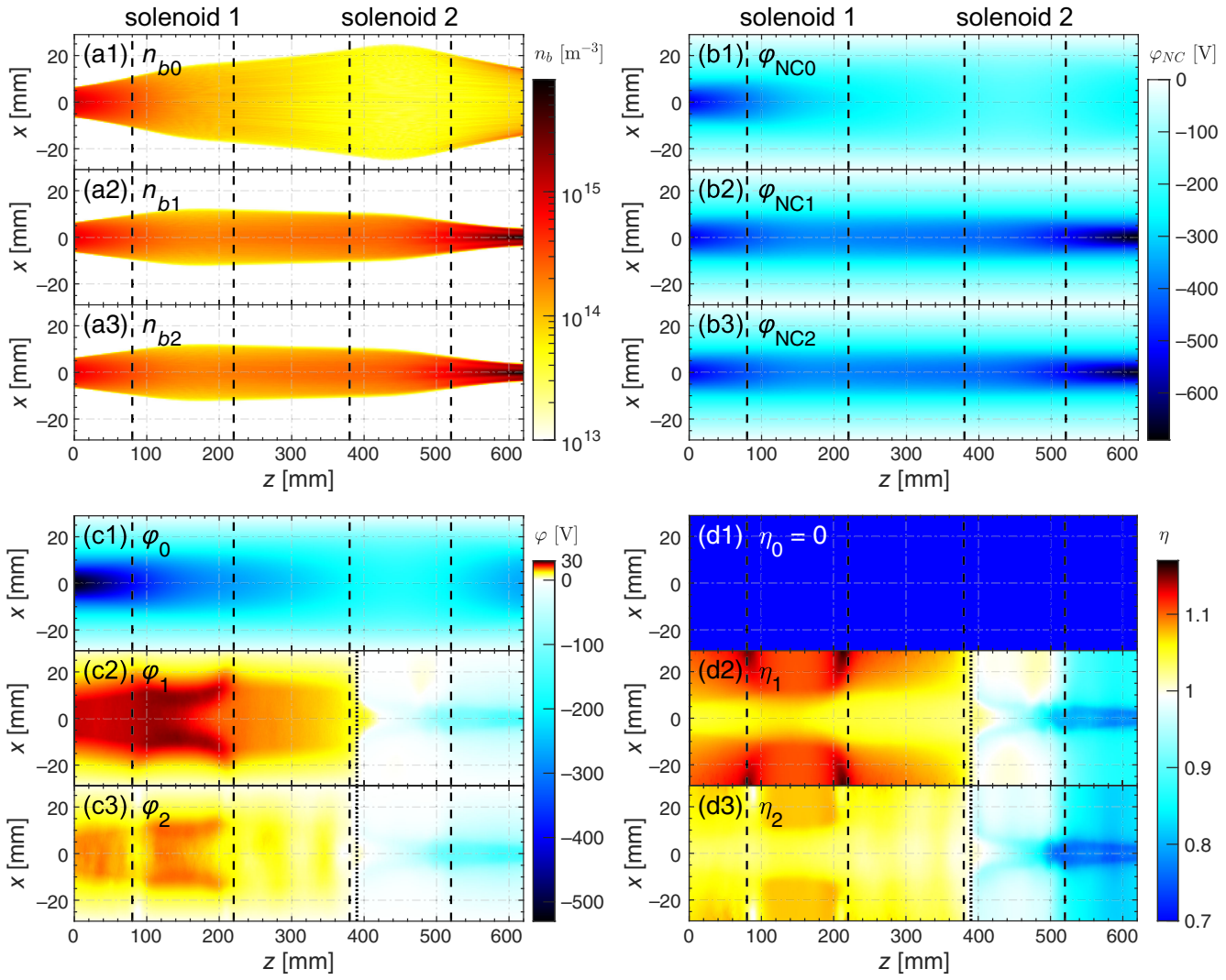


FIG. 3. Distributions of (a) the beam densities, (b) φ_{NC}, (c) the potentials, and (d) the SCCDs when the steady state is achieved in different cases: (1) without secondary particles (case 0), (2) with secondary ions and without secondary electrons (case 1), and (3) with both secondary ions and electrons (case 2). These results are observed at the plane $y = 0$. Dashed lines are the boundaries of solenoid magnetic fields. Dotted lines at $z = 390$ mm divide the simulation area into the overcompensation region (left) and the undercompensation region (right).

the beam goes forward due to beam divergence before solenoid 2. The growth of φ_{NC1} in Fig. 3(b2) appears to be slower, attributed to the SCC caused by secondary ions. The beam focusing results in the minimum of φ_{NC1} (-655 V) occurring at $z = 600$ mm. Case 2 exhibits a slightly lower φ_{NC} than case 1, with $\varphi_{NC1} - \varphi_{NC2} < 8$ V. The resemblance between Figs. 3(b2) and 3(b3) is related to their analogous beam distributions.

However, secondary electrons have a significant impact on the observed potential [Fig. 3(c)] and SCCD [Fig. 3(d)] in systems at equilibrium. The potentials in both case 1 [Fig. 3(c2)] and case 2 [Fig. 3(c3)] are higher than φ_0 in case 0 [Fig. 3(c1)]. Actually, when no secondary particles exist, the beam is fully uncompensated $\varphi_0 = \varphi_{NC0}$ in case 0. The potential values in case 2 are lower than those in case 1 due to the presence of extra electrons. Furthermore, the results indicate that the simulation area can be divided into an overcompensation region ($z < 390$ mm) and an undercompensation region ($z > 390$ mm) in Figs. 3(c2) and 3(c3). In the overcompensation region, secondary ions accumulate under magnetic confinement, leading to a positive potential. The maximum potential is located in solenoid 1, measuring 26 V in Fig. 3(c2) and 19 V in Fig. 3(c3), which is not high enough to confine the electrons in reactions (2) and (3) with an initial energy of 27 eV (about 1/1838 of 50 keV). This indicates that electrons detached from beam ions have minimal impact on the SCC. In contrast, the undercompensation region exhibits a negative potential due to (1) the attraction of secondary ions by the forward-moving beam, causing them to escape from the right boundary; and (2) the difficulty for secondary ions to remain at the center when the beam is focused and has a small radius. The potentials in this region show slight variations between Figs. 3(c2) and 3(c3), which will be further discussed below.

According to Eq. (7), the SCCDs in three cases are calculated in Fig. 3(d). The SCCD is always zero since the SCC effect is not considered in case 0 [Fig. 3(d1)]. By comparing the SCCDs in case 1 [Fig. 3(d2)] with those in case 2 [Fig. 3(d3)], it is found that electrons in case 2 weaken the SCC effect ($\eta_2 < \eta_1$), making the SCCD closer to 100% in the overcompensation region and even lower in the undercompensation region. Note that when a gas with a heavier atomic mass, such as Ar, is used, the overcompensation becomes more pronounced, resulting in a much smaller undercompensation region (see Appendix C).

To quantitatively compare the potentials, transverse and longitudinal profiles at various positions are given in Figs. 4(a)–4(c).

These results reflect different SCC situations in the overcompensation region and undercompensation region, as well as the influence of secondary electrons. In the overcompensation region, the transverse profile of the observed potential has a double-peak structure, resulting from the magnetic confinement on the secondary ions. The observed potential in case 2 (φ_2) is positive and is

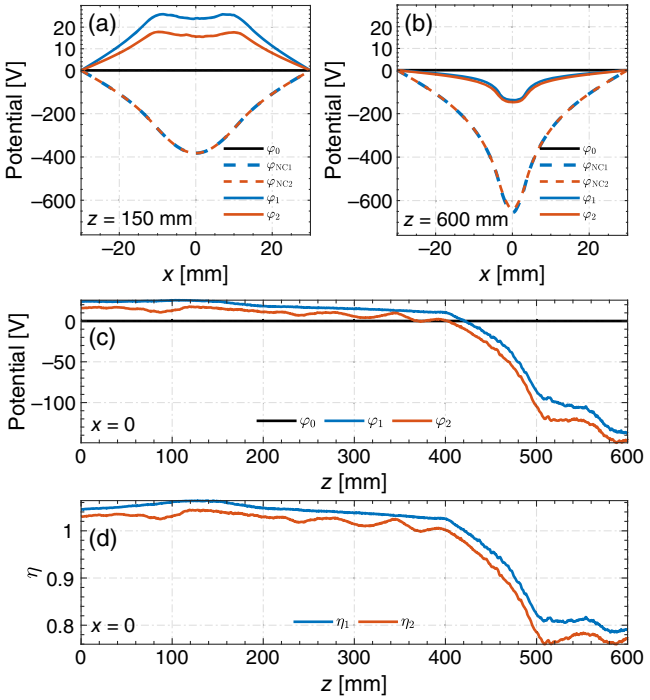


FIG. 4. Potentials and SCCDs at different positions at $t = 50$ μs. (a) and (b) are the transverse distributions of potentials at $z = 150$ and 600 mm, respectively. The longitudinal distributions of potentials and SCCDs are shown in (c) and (d). φ_0 is the potential of full compensation, φ_{NC} is the potential of no compensation, and φ is the observed potential. The subscript numbers 1 and 2 represent case 1 (without electrons) and case 2 (with electrons), respectively.

approximately half of that in case 1 (φ_1) because secondary electrons greatly reduce the potential difference between φ and φ_0. Conversely, in the undercompensation region, the minimum of the observed potential is at the center. φ_1 and φ_2 are below zero, with a small difference of less than 11 V, compared to the minimum potential $\varphi_{NC\,min} = -655$ V. The profile of φ_{NC} is sharper in Fig. 4(b) compared to Fig. 4(a) because of a smaller radius and higher beam density at $z = 600$ mm. The longitudinal profiles of potential and SCCD [Figs. 4(c) and 4(d)] exhibit similar trends. The values in case 2 are apparently lower than those in case 1. The results above demonstrate an obvious decline in the potential and SCCD when electrons are considered.

B. Space charge density

The SCCD difference between case 1 and case 2 results from different distributions of the space charge. Figure 5 compares the charge densities of the H^- beam, secondary ions, and secondary electrons, and the total charge density of all particles in case 1 and case 2 when the steady state is reached.

Figures 5(a1), 5(b1), and 5(d1) correspond to case 1, while the rest refer to case 2. These area charge densities are

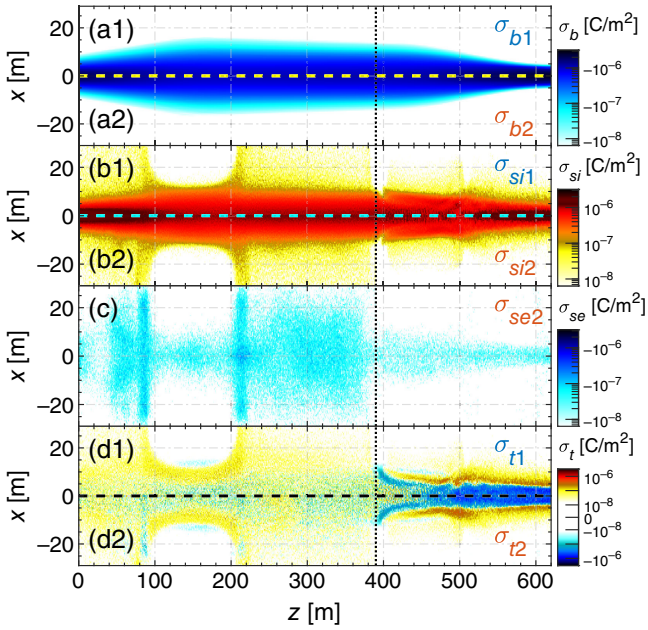


FIG. 5. Area charge densities of (a) the H^- beam, (b) the secondary ions, (c) the secondary electrons, and (d) all charged particles at $t = 50$ μs. Numbers 1 and 2 in the labels and subscripts represent case 1 (above the dashed line) and case 2 (below the dashed line). Dotted lines at $z = 390$ mm divide the simulation area into the overcompensation region (left) and the undercompensation region (right).

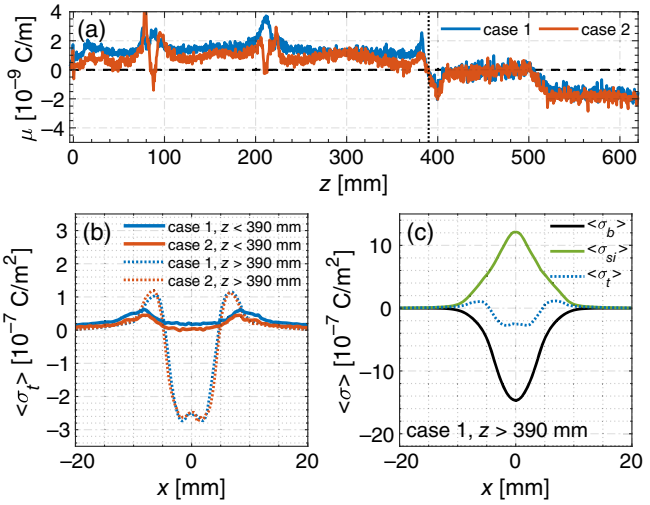


FIG. 6. Several charge density profiles at $t = 50$ μs. (a) The linear charge density of all particles in the longitudinal direction. (b) The average total area charge density in the x direction. (c) The average charge density of beam particles and secondary ions in the undercompensation region.

the integration of volume charge densities along the y direction. In the overcompensation region, the beam [see Fig. 5(a)] and the secondary ions [see Fig. 5(b)] have similar distribution and number density. Considerable secondary ions outside the beam are confined by the magnetic field of solenoid 1, resulting in high SCCDs around the beam [see Figs. 3(d2) and 3(d3)]. In the undercompensation region; however, the secondary ions can leave from the right boundary, leading to a lower density compared to the beam density. Case 1 and case 2 have overall similar distributions of the beam and the secondary ions. Nonetheless, the number of secondary ions in case 2 are higher due to the attraction from electrons, which will become more evident in later results of the particle number evolution.

Secondary electrons are mainly distributed in the overcompensation region [see Fig. 5(c)]. This is because they can respond to the positive potential field very quickly due to their much lower mass and higher velocity compared to the H_2^+ ions. The small mass of electrons also makes them more easily captured by the magnetic field, leading to a high electron density on either side of solenoid 1. In the undercompensation region, the negative electric potential results in few electrons remaining, as they are quickly expelled by the electric field.

The total charge density [Fig. 5(d2)] is lower when secondary electrons are considered in the SCC, compared with the result in Fig. 5(d1). In the overcompensation region, case 2 exhibits a reduced total charge density because of the accumulation of secondary electrons, particularly around the edges of solenoid 1. However, in the undercompensation region, solenoid 2 focuses the quasiparallel beam, leading to an increase in beam density. Meanwhile, secondary ions continuously escape from the right boundary, resulting in a negative charge density at the center. Since the number of electrons in the undercompensation region is small, distinguishing between the total charge distributions in case 1 and case 2 is challenging.

To facilitate comparison of these densities, calculating the integral or average of the area charge densities would be more convenient. The linear charge density results in the z direction [Fig. 6(a)] show an obvious decline in total charge in the overcompensation region in case 2, particularly around solenoid 1.

While in the undercompensation region, slightly more negative charge is observed in case 2. Similar conclusions are drawn from the average total area charge density in the x direction [see solid lines in Fig. 6(b)]. Note that the most obvious phenomenon of overcompensation occurs around the beam, rather than in the central region. In the undercompensation region, the total charge density is positive around the beam but negative in the center [see Fig. 6(c)]. This is not due to a greater number of secondary ions at the beam edge than in the center, but rather because the distribution range of secondary ions is wider than that of the ion beam, a fact also confirmed by Ref. [4].

Efforts are also made to check the beam dynamics. Figure 7 shows how the space charge density and the transverse electric field at $z = 300$ mm change as SCC develops in case 1. Both the charge density and the electric

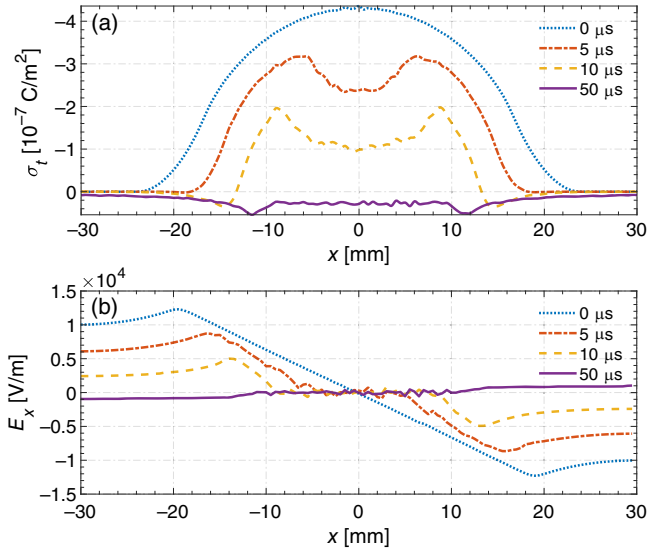


FIG. 7. Time evolution of (a) the total charge density and (b) the transverse electric field at $z = 300$ mm.

field keep falling with time before the overcompensation occurs. When the steady state is eventually achieved, the space charge becomes positive. The electric field reverses direction with significantly reduced strength, as a result of the positive potential in the overcompensation region [see Fig. 4(a)].

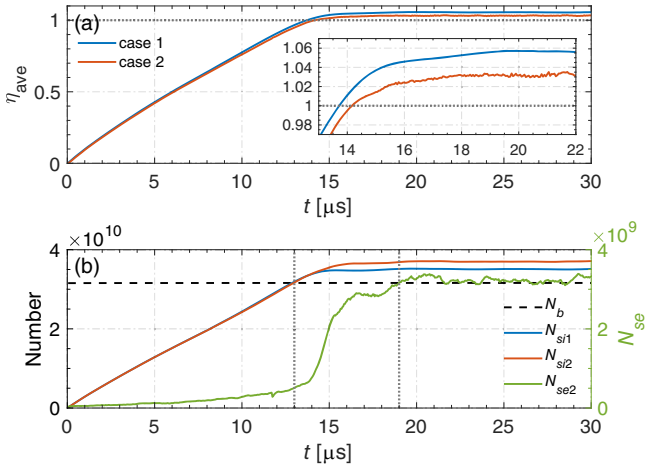


FIG. 8. Time evolution of (a) SCCDs and (b) charged particle numbers in the overcompensation region.

C. Time evolution of SCCDs and particle numbers

While the SCCD and spatial distributions of charged particles are essential for the beam transport in an equilibrium state, it is also important to understand how these quantities change over time, as they reflect the buildup of the SCC. In this section, we discuss the increase of SCCD and secondary particle number in case 1 and case 2. The average SCCD is used to describe the overall SCC level of the beam. It is defined as

$$\eta_{\text{ave}} = \sum_i \sum_j \sum_k n(x_i, y_j, z_k)\eta(x_i, y_j, z_k) / \sum_i \sum_j \sum_k n(x_i, y_j, z_k), \tag{8}$$

where $n(x_i, y_j, z_k)$ and $\eta(x_i, y_j, z_k)$ are the beam density and SCCD in position (x_i, y_j, z_k).

The SCCD continues to increase, although the rate of increase is decreasing [see Fig. 8(a)].

This phenomenon occurs due to the increased likelihood of secondary ions penetrating the potential barrier and reaching the boundary as the SCCD grows. The time required for the SCCD to reach 100% is 13.7 μs in case 1 and 14.2 μs in case 2. Both are close to the predicted compensation time of 11 μs by Eq. (4). After achieving 100%, the SCCD continues to increase because of overcompensation. In case 1, η_{ave} experiences an additional growth of 5.6%, while in case 2, this increase is around 3.2%. Secondary electrons can reduce the increase (over 100%) of SCCD by more than 42%.

The evolution of charged particles [Fig. 8(b)] is similar to that of SCCD except for the behavior of electrons. The number of secondary ions equals the beam particle number ($N_b = 3.16 \times 10^{10}$) at 13.0 μs($1.18\tau$) and keeps rising until it reaches $1.12N_b$ in case 1 and $1.18N_b$ in case 2. Electrons contribute to a lower SCCD but meanwhile a higher number of secondary ions. The increase of electrons can be divided into three stages. In stage one ($t < 1.18\tau$), the beam is undercompensated, and electrons grow steadily at a very low rate. Most electrons are expelled to the wall, and only a few remain, resulting in the SCCD in case 2 being slightly lower than in case 1. In stage two ($1.18\tau < t < 1.73\tau$), the growth rate of electrons increases significantly because the spatial potential is above zero and continues to rise, preventing the electrons from being driven to the wall by the transverse electric field. The growth rate of electrons gradually decreases as their number increases to $0.1N_b$. In stage three ($t > 1.73\tau$), equilibrium is achieved, and the number of charged particles remains nearly constant. The final total charge in case 1 and case 2 reaches $0.12N_be$ and $0.08N_be$, respectively, representing a 50% decrease in the net charge when electrons are considered.

D. Beam parameters

Given the notable suppression of overcompensation and the evident decline in the SCCD in case 2, this section examines the impact of electrons on the beam parameters.

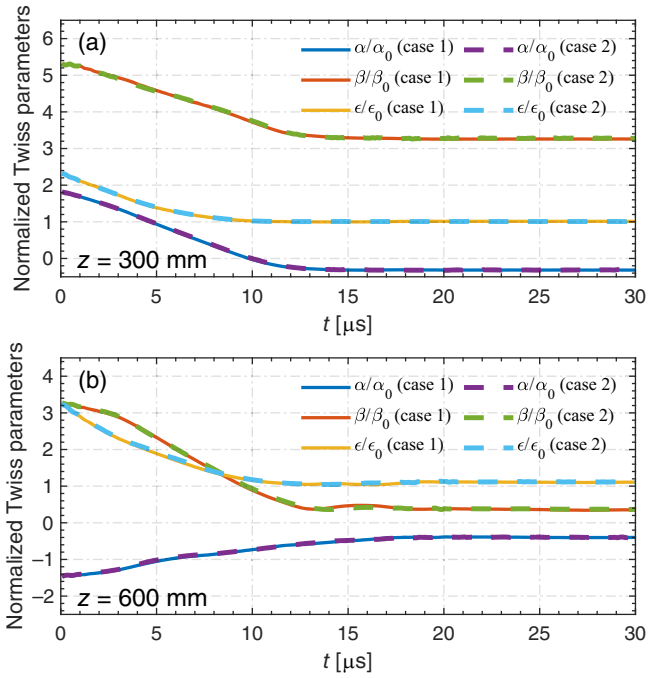


FIG. 9. Time evolution of the normalized Twiss parameters of the beam at (a) $z = 300$ mm and (b) 600 mm.

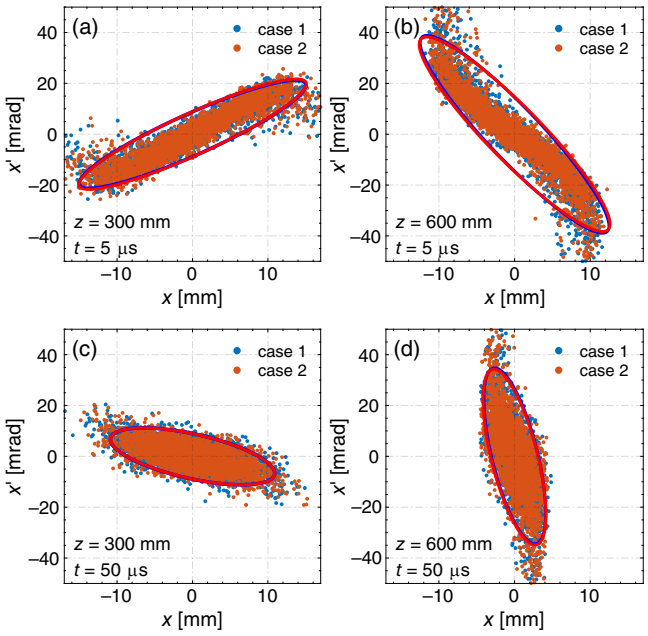


FIG. 10. Phase space diagrams of the H^- beam at different locations and moments in case 1 and case 2. The curves are 5-rms ellipses.

On the one hand, the time evolution of the beam in case 1 and case 2 is very similar. Each normalized Twiss parameter of the beam changes with time following the same pattern, as shown in Fig. 9.

Compared with the large emittance when SCCD equals zero at $t = 0$ ($> 3\epsilon_0$), the final emittance differences between two cases are too tiny to distinguish. Note that the beam emittance experiences a remarkable decrease as the SCC develops. Also, the final phase space distributions of the ion beam (Fig. 10) in case 1 and case 2 are generally similar. The H^- ions rotate clockwise from $t = 5$ to 50 μs as a result of beam convergence.

But on the other hand, the spatial increase of beam emittance differs in these two cases, as illustrated in Fig. 11(a). In the overcompensation region ($z = 300$ mm), since the SCCD exceeds 100%, the space charge effect on the beam is relatively weak, leading to minimal emittance growth compared to the initial emittance $\epsilon_0 = 0.1991$ mm mrad.

However, the difference in the emittance growth between case 1 (0.0028 mm mrad) and case 2 (0.0018 mm mrad) is considerable (see Table I). The emittance growth in case 2 decreases by about 35% due to the presence of secondary electrons, which contribute to a more uniform and even potential distribution.

Noticing the small difference in emittance growth at $z = 300$ mm between case 1 and case 2 in Table I, we decided to examine another beam with distinct initial parameters to investigate if this difference is due to the secondary electrons or the numerical resolution of the simulation process. This new beam has a lower initial normalized rms emittance of $\epsilon_{\rm rms} = 0.0896$ mm mrad with Twiss parameters $\alpha = -5.784$, $\beta = 0.868$ mm/mrad, and $\gamma = 39.711$ mrad/mm. The simulation results of beam parameters are listed in Table I, which confirm a lower beam emittance growth at $z = 300$ mm in case 2 (0.0005 mm mrad) compared to case 1 (0.0015 mm mrad). The presence of electrons does lead to a smaller beam emittance growth in the overcompensation region.

However, in the undercompensation region (z=600mm), electrons reduce the SCCD of the beam, resulting in a

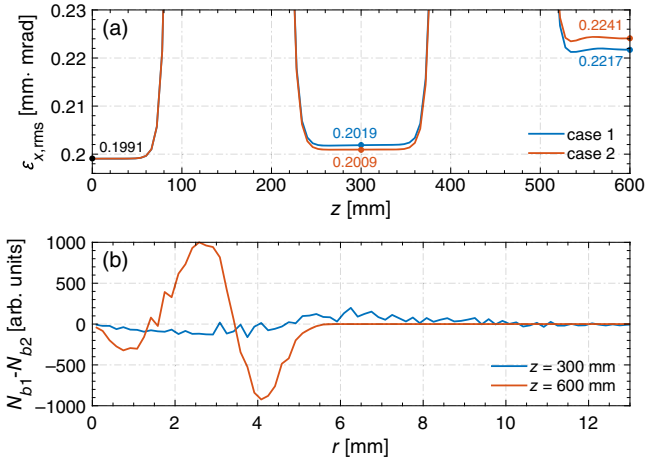


FIG. 11. (a) Normalized rms emittance in the x direction as a function of distance and (b) differences in the number of beam particles between case 1 and case 2 at $z = 300$ and 600 mm. Data are collected at $t = 50$ μs.

TABLE I. Twiss parameters, normalized rms emittance, and radius of the negative hydrogen ion beam in case 1 and case 2 when the steady state is reached.

ϵ_0 (mm mrad)	z (mm)	Electron consideration	α	β (m/rad)	γ (rad/m)	$\epsilon_{x,\mathrm{rms}} - \epsilon_0$ (mm mrad)	r (mm)
0.1991	300	No (case 1)	0.742	1.214	1.278	0.0028	10.39
	300	Yes (case 2)	0.749	1.218	1.281	0.0018	10.38
	600	No (case 1)	0.855	0.155	11.141	0.0226	3.68
	600	Yes (case 2)	0.865	0.159	11.005	0.0250	3.75
0.0896	300	No (case 1)	2.078	2.887	1.842	0.0015	10.00
	300	Yes (case 2)	2.139	2.931	1.902	0.0005	10.00
	600	No (case 1)	2.060	0.286	18.349	0.0083	3.15
	600	Yes (case 2)	2.055	0.316	16.554	0.0098	3.34

larger emittance growth in case 2. From $z = 300$ to 600 mm, the emittance increases by 0.0198 mm mrad in case 1 and 0.0232 mm mrad in case 2. The differences in beam particle number between case 1 and case 2 at $z = 300$ and 600 mm in Fig. 11(b) indicate that more beam ions are attracted to the edge of the beam in case 1 than in case 2 in the overcompensation region. While in the undercompensation region, an opposite distribution occurs with more particles concentrated in the center in case 1. The difference in beam particle distribution results from the varying transverse potential distributions [Figs. 4(a) and 4(b)] and explains the aforementioned emittance difference.

Though these differences can be analyzed statistically, details would be hard to discern from the phase space diagrams in Fig. 10, which are typically obtained through experimental measurement. When focusing on the beam itself, regardless of the precision of potential and SCCD, there will not be a large calculation deviation even if secondary electrons are not considered as in case 1. This suggests that beam optics simulations without electrons, where significant overcompensation occurs are still valid. After considering secondary electrons, more accurate distributions of secondary particles and beam Twiss parameters can be obtained.

V. CONCLUSIONS

To summarize, we report the suppression of overcompensation by secondary electrons when a 40 mA negative hydrogen ion beam at 50 keV passes through 3.36 mPa residual hydrogen. Using a practical beam optics calculation code combined with a model for secondary particle production and tracking, the overcompensation process of negative ion beams is studied via simulation. To figure out the influence of electrons on the SCC, which is often neglected in beam optics calculations, simulations without electrons (case 1) and with electrons (case 2) are carried out. It is found that secondary electrons can effectively level the potential and reduce the SCCD in the overcompensation region. More secondary ions are observed in case 2, yet the total charge density is lower due to the suppression of overcompensation. The accumulation of secondary electrons can be divided into three stages: the low-growth-rate stage, the high-growth-rate stage, and the equilibrium stage. Different patterns of emittance growth in both cases are analyzed, showing that case 2 has an emittance growth 35% lower than case 1 in overcompensation region, although the emittance at the exit in case 2 exceeds that in case 1. More accurate beam optics simulations can be achieved by incorporating the effects of electrons. Future work will involve improving simulation accuracy by considering close collisions and thermalization of particles.

ACKNOWLEDGMENTS

The authors express their gratitude to Taneli Kalvas for providing the IBSimu code through the webpage, which facilitated the beam optics simulation in this study. This work was supported by China Postdoctoral Science Foundation (Grant No. 2024M761760), Guangdong Basic and Applied Basic Research Foundation (Grant No. 2024B1515120028), and Xiejialin Foundation (Grant No. E55468U2).

DATA AVAILABILITY

The datasets generated and analyzed during the current study are available from the corresponding authors upon reasonable request. The simulation details are available from the corresponding author on reasonable request.

APPENDIX A: IONIZATION CROSS SECTION

The cross sections for H_2 and Ar being ionized by a H^- ion [see reaction (1) for the ionization of H_2] are given in Fig. 12.

The ionization cross sections for H^- impact ionization are calculated by adding the contributions of one H^+ [18] and two electrons [19–21] for the lack of available ionization cross section data for residual gases by H^-. At an energy of 50 keV, the ionization cross section is 3.66×10^{-20} m^2 for H_2 and 9.50×10^{-20} m^2 for Ar.

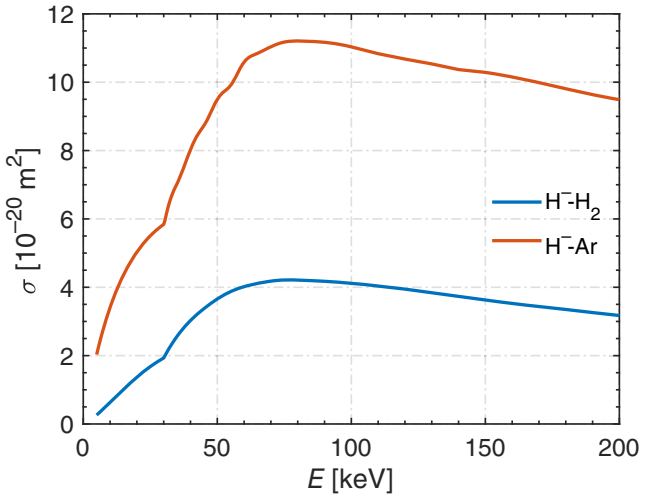


FIG. 12. Ionization cross section as a function of beam energy from 0 to 200 keV for H_2 and Ar.

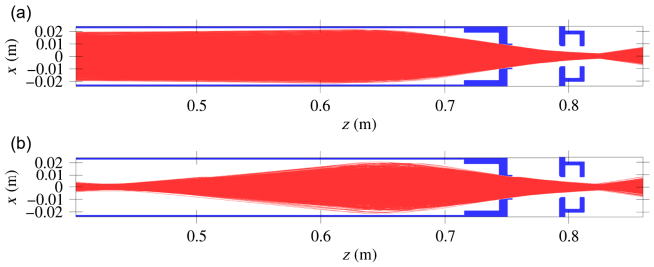


FIG. 13. Trajectories of H^- ions of two beam transport schemes. Before solenoid 2 ($z = 662$ mm) the beam is (a) parallel and (b) crossed, respectively.

APPENDIX B: CODE BENCHMARKS

We conducted several benchmark simulations which yielded results consistent with the experimental data collected from the ion source test stand at China Spallation Neutron Source (CSNS).

Similar to the model introduced in Sec. III, the LEBT on the ion source test stand at CSNS also includes two solenoids. By adjusting the current of the solenoids, one can achieve either a parallel beam or a crossed beam between them. These two schemes have been studied through experiments and simulations. Figure 13 shows the simulated beam trajectories of two schemes from the middle of two solenoids ($z = 400$ mm) to the right boundary.

Experimentally, the phase space diagram and Twiss parameters of the ion beam in the LEBT can be measured by a double-slit scanner at two positions. One is between the two solenoids (before solenoid 2), and the other is at the exit of the LEBT (after solenoid 2). They are positioned at $z = 400$ mm and $z = 810$ mm from the plasma emission aperture ($z = 0$), respectively. When the parallel beam transport scheme is applied, the beam phase space diagrams of a 36 mA negative hydrogen ion beam are measured before and after solenoid 2 [Figs. 14(a) and 14(b)].

The results of the crossed beam are shown in Figs. 14(c) and 14(d). The pressure of 3.5 mPa is obtained by a vacuum gauge at $z = 400$ mm.

In the benchmarks, we utilize the beam measurements taken before solenoid 2 [Figs. 14(a) and 14(c)] as the input beam parameters to closely match the experiment. The input beams are generated based on the measured Twiss parameters (see Table II) and exhibit a Gaussian distribution [see Figs. 14(e) and 14(g)]. Random number generators are used to set the position and velocity of the beam particles, so the Twiss parameters of input beams in simulations may differ a bit from those in experiments. However, their beam ellipses and the emittances are almost the same.

Simulation results indicate that both the parallel beam and the crossed beam are highly compensated in 3.5 mPa hydrogen, with an average SCCD over 90%. The inside

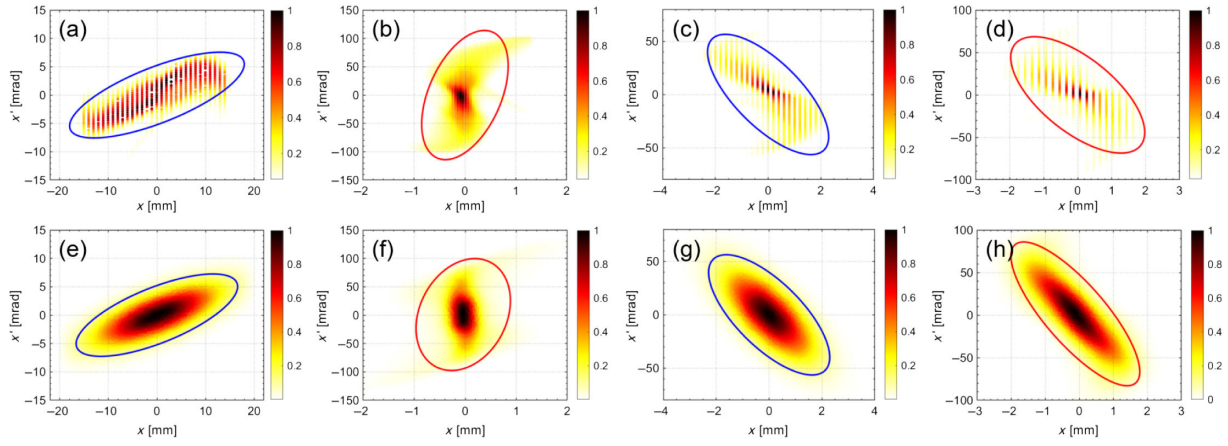


FIG. 14. The $x - x'$ phase space diagrams of (a)–(d) measured beams and (e)–(h) corresponding simulated beams. (a) and (b) depict the phase space diagrams of a parallel beam before and after solenoid 2, while (c) and (d) represent a crossed beam. The colored curves represent the 5-rms ellipses.

TABLE II. Twiss parameters, normalized rms emittance, and ellipse tilt angle of the negative hydrogen ion beam in experiments and simulations.

Type	Beam scheme	Case	z (mm)	α	β (m/rad)	γ (rad/m)	$\epsilon_{x,\mathrm{rms}}$ (mm mrad)	θ (rad)
Experiment	Parallel	(a)	400	−1.14	3.68	0.62	0.180	0.32
	Parallel	(b)	810	−0.49	0.01	145.69	0.185	1.57
	Crossed	(c)	400	1.00	0.06	34.78	0.189	−1.54
	Crossed	(d)	810	0.85	0.04	45.48	0.214	−1.55
Simulation	Parallel	(e)	400	−0.97	3.18	0.61	0.179	0.32
	Parallel	(f)	810	−0.26	0.01	110.07	0.182	1.57
	Crossed	(g)	400	1.00	0.06	34.75	0.188	−1.54
	Crossed	(h)	810	1.35	0.04	74.92	0.197	−1.55

diameter of the LEBT pipe in Fig. 13 is 45 mm, lower than the transverse width of 60 mm in Fig. 2(a), which results in more secondary particles being absorbed. The corresponding phase space distributions at the exit of the LEBT ($z = 810$ mm) are given in Figs. 14(f) and 14(h). Compared with the phase space diagrams in Figs. 14(b) and 14(d), our simulation results generally align with the experimental data. Due to a better fitting of the input beam, the parallel beam exhibits a phase space distribution closer to the experiment results compared to the crossed beam. The output beam parameters of simulations, especially the emittance and ellipse tilt angle, also agree with those of experiments in Table II. These benchmark results indicate that our code can be effectively applied to beam optics in the LEBT.

APPENDIX C: SCCD DISTRIBUTIONS IN AR

The SCCD shows an obvious increase when a gas with a heavier atom mass is used. Compared to H_2 [see Figs. 3(d2) and 3(d3)], Ar (see Fig. 15) not only leads to a higher level of SCCD but also eliminates the undercompensation region, which tends to show up at the exit.

The suppression of overcompensation by electrons is also clear in Ar. The SCCD exhibits a maximum decrease of 30% in Fig. 15(b). Note that the electrons stripped from beam ions cannot escape from the positive potential field with such strong overcompensation. Reactions (2) and (3) should also be considered. But the results in Fig. 15 can still demonstrate a more pronounced overcompensation in Ar than in H_2 as well as the suppression of overcompensation by electrons.

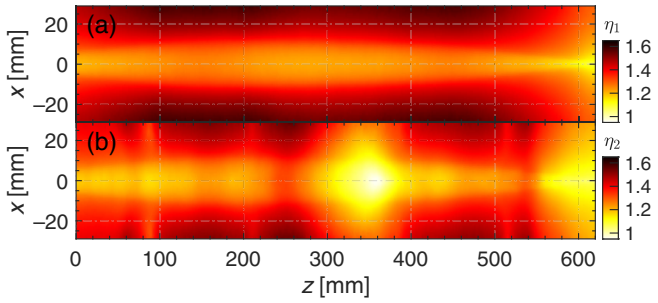


FIG. 15. SCCD distributions when the negative hydrogen ion beam passes through high-density Ar in (a) case 1 and (b) case 2. Except for the gas type, all settings are consistent with those in the main text.

[1] R. Keller, R. Thomae, M. Stockli, and R. Welton, Design, operational experiences and beam results obtained with the H^- ion source and LEBT at Berkeley Lab, AIP Conf. Proc. **639**, 47 (2002).
[2] W. Chen, H. Li, H. Liao, Y. Lu, X. Cao, S. Liu, Y. Xiao, and B. Chen, RF-driven H^- sources of long life-time and new LEBT developed at CSNS, J. Phys. Conf. Ser. **2743**, 012040 (2024).
[3] A. Ueno, J-PARC H^- ion source and space-charge neutralized LEBT for 100-mA high energy and high duty factor LINACs, Rev. Sci. Instrum. **91**, 033312 (2020).
[4] C. A. Valerio-Lizarraga, I. Leon-Monzon, and R. Scrivens, Negative ion beam space charge compensation by residual gas, Phys. Rev. ST Accel. Beams **18**, 080101 (2015).
[5] H. Liao, W. Chen, H. Li, B. Chen, Y. Xiao, Y. Lv, X. Cao, S. Liu, J. Peng, X. Feng, and S. Liu, Removal of stripped protons produced in low-energy beam transport for superconducting linac, Phys. Rev. Accel. Beams **28**, 023502 (2025).
[6] J. Ishikawa, F. Sano, and T. Takagi, Ion-beam extraction with ion space-charge compensation in beam-plasma type ion-source, J. Appl. Phys. **53**, 6018 (1982).
[7] R. Becker, Space-charge compensation of thermal beams, Nuovo Cimento Soc. Ital. Fis. **106A**, 1613 (1993).
[8] P. Veltri, M. Cavenago, and G. Serianni, Study of space charge compensation phenomena in charged particle beams, Rev. Sci. Instrum. **83**, 02B709 (2012).
[9] P. Veltri, M. Cavenago, and G. Serianni, Spatial characterization of the space charge compensation of negative ion beams, AIP Conf. Proc. **1515**, 541 (2013).
[10] E. Surrey, Space charge neutralization in the ITER negative ion beams, AIP Conf. Proc. **925**, 278 (2007).

[11] S. V. Dudin and D. V. Rafalskyi, On the simultaneous extraction of positive ions and electrons from single-grid ICP source, Europhys. Lett. **88**, 55002 (2009).

[12] A. BenIsmail, R. Duperrier, D. Uriot, and N. Pichoff, Space charge compensation studies of hydrogen ion beams in a drift section, Phys. Rev. ST Accel. Beams **10**, 070101 (2007).

[13] F. Gérardin, N. Chauvin, A. Chancé, O. Napoly, N. Pichoft, D. Uriot, M. Baylac, D. Bondoux, and F. Bouly, Space charge compensation in low energy beam lines, in *Proceedings of the International Particle Accelerator Conference (IPAC'16), Busan, Korea* (JACoW, Geneva, Switzerland, 2016), Vol. 7, pp. 3055–3057, 10.18429/JACoW-IPAC2016-WEPOY033.

[14] D. Noll, M. Droba, O. Meusel, U. Ratzinger, and K. Schulte, Simulation of space-charge compensation of a low-energy proton beam in a drift section, in *Proceedings of the ICFA Advanced Beam Dynamics Workshop on High-Intensity and High-Brightness Hadron Beams (HB'16), Malmö, Sweden* (JACoW, Geneva, Switzerland, 2016), Vol. 57, pp. 458–462, 10.18429/JACoW-HB2016-WEPM8Y01.

[15] C. A. Valerio-Lizarraga, Emittance growth due to space charge compensation and beam intensity instabilities in negative ion beams, Phys. Rev. Accel. Beams **21**, 030101 (2018).

[16] T. Kalvas, O. Tarvainen, T. Ropponen, O. Steczkiewicz, J. Arje, and H. Clark, IBSimu: A three-dimensional simulation software for charged particle optics, Rev. Sci. Instrum. **81**, 02B703 (2010).

[17] J. Sherman, E. Pitcher, R. Stevens, and P. Allison, H^- beam neutralization measurements in a solenoidal beam transport-system, AIP Conf. Proc. **287**, 686 (1992).

[18] M. E. Rudd, R. D. Dubois, L. H. Toburen, C. A. Ratcliffe, and T. V. Goffe, Cross-sections for ionization of gases by 5-4000-keV protons and for electron-capture by 5-150-keV protons, Phys. Rev. A **28**, 3244 (1983).

[19] H. Straub, P. Renault, B. Lindsay, K. Smith, and R. Stebbings, Absolute partial cross sections for electron-impact ionization of H_2, N_2, and O_2 from threshold to 1000 eV, Phys. Rev. A **54**, 2146 (1996).

[20] R. Rejoub, B. Lindsay, and R. Stebbings, Determination of the absolute partial and total cross sections for electron-impact ionization of the rare gases, Phys. Rev. A **65**, 042713 (2002).

[21] K. Tokesi and R. D. Dubois, Ionization cross sections of hydrogen molecule by electron and positron impact, Int. J. Mol. Sci. **25**, 3410 (2024).